Nuclear Instruments and Methods in Physics Research A 756 (2014) 45–54

Contents lists available at ScienceDirect

Nuclear Instruments and Methods in Physics Research A

journal homepage: www.elsevier.com/locate/nima

Characterization of a cubic EJ-309 liquid scintillator detector

A. Tomanin [a,*], J. Paepen [b], P. Schillebeeckx [b], R. Wynants [b], R. Nolte [c], A. Lavietes [d]

[a] European Commission – Joint Research Centre – Institute for TransUranium Elements (EC-JRC-ITU), Via E. Fermi 2749, 21020 Ispra (VA), Italy
[b] European Commission – Joint Research Centre – Institute for Reference Materials and Measurements (EC-JRC-IRMM), Retieseweg 111, B-2440 Geel, Belgium
[c] Physikalische-Technishe Bundesanstalt (PTB), Bundesallee 100, 38116 Braunschweig, Germany
[d] International Atomic Energy Agency (IAEA), Vienna, Austria

ARTICLE INFO

Article history:
Received 15 December 2013
Received in revised form
17 March 2014
Accepted 18 March 2014
Available online 26 March 2014

Keywords:
Liquid scintillator
Neutron detector
Pulse shape discrimination (PSD)
Response functions
EJ-309
Time-of-flight (TOF)

ABSTRACT

A cubic EJ-309 liquid scintillator of 10 cm width has been characterized for its response to γ-rays and neutrons. Response functions to γ-rays were measured with calibrated radionuclide γ-ray sources in the energy range from 400 keV to 6 MeV. Response functions for neutrons were obtained from measurements at the PTB Van de Graaff accelerator with quasi-monoenergetic neutron beams in the energy range from 500 keV to 2.7 MeV, and at the PTB cyclotron with time-of-flight (TOF) measurements in the energy range from 2.5 to 14 MeV. The light output and resolution functions for electrons and protons were derived by a least squares adjustment to experimental data using theoretical response functions determined with Monte Carlo simulations. The simulated response function for neutron was validated by results of measurements with an AmBe neutron source which was characterized for its total neutron intensity. The results indicate that the cubic EJ-309 detector is suitable for use in mixed γ-ray and neutron fields.

1. Introduction

The detection of neutrons is used in various fields as a signature of the presence of fissile and special nuclear materials. Applications of interest include nuclear security, where large neutron detectors are used to reveal illicit trafficking of nuclear materials, and nuclear safeguards, where the role of neutron detection is crucial for the verification of facilities' nuclear material inventories for timely detection of material diversion.

Currently deployed detectors rely on the use of ^{3}He gas, due to both the high cross-section for the ^{3}He(n,p)^{3}H reaction at thermal neutron energy and the low sensitivity to γ-rays. For nuclear security and safeguards applications, ^{3}He gas detectors are mostly embedded in a moderator material to increase their detection efficiency to fast neutrons from fissions and (α,n) reactions. The increased demand for ^{3}He-based neutron detectors, in particular for nuclear security applications, coupled with the limited production of ^{3}He, created the need for alternative neutron detection solutions.

Liquid scintillators have been proposed as a suitable alternative to ^{3}He for neutron detection. They are sensitive to fast neutrons, which are mainly detected via elastic scattering with hydrogen, and can be used in the presence of a mixed-particles radiation field when pulse shape discrimination (PSD) techniques are applied to discriminate pulses generated by different incident particles.

For many decades, liquid scintillators have been used as neutron detectors for a variety of applications including basic nuclear physics studies [1,2], nuclear technology diagnostic [3,4], and radiation protection and dosimetry [5]. A particular application of liquid scintillators is neutron spectroscopy [5–7], both with time-of-flight [8] and pulse-height spectroscopy [9,10] techniques. The former relies on the good timing resolution of liquid scintillator detectors. The latter is based on spectra unfolding [11] and requires accurate response functions of the detector [5,7].

The use of more traditional liquid scintillators, such as NE213, BC-501A or its equivalent EJ-301, has been longly limited to supervised applications due to the hazardous nature related to the low flash point (26 °C) of these fluids. Only the recent advent of liquids with a high flashpoint and low toxicity, such as EJ-309 (ELJEN Technology [12], with a flash point of 144 °C), coupled with the advent of fast electronics for real-time PSD [13,14], has made this technology suitable for unattended use in an industrial environment [15].

Due to the characteristic fast response to neutrons, liquid scintillators have found a particular application in the replacement of ^{3}He-based neutron detection systems used for nuclear safeguards [16,17]. Furthermore, the production technique does not pose a-priori limitations on the size of the detectors, as in the case of crystal detectors. Hence, they can replace ^{3}He detectors if a high detection efficiency is required, as in the case of nuclear security applications.

* Corresponding author. Tel.:+39 0332 786179; fax: +39 0332 785072.
E-mail address: alice.tomanin@jrc.ec.europa.eu (A. Tomanin).

http://dx.doi.org/10.1016/j.nima.2014.03.028
0168-9002/

Nevertheless, constraints on the size and geometry of the cells are imposed by the light propagation and the pulse shape for particle discrimination. Previous research have focused on cylindrical scintillator cells [15,18,19], with a maximum cell diameter of 12.7 cm [19,20]. In this paper, the characterization of a cubic EJ-309 liquid scintillator cell is presented. An array of such detectors is intended to be used in a safeguards application, for which a cubic cell geometry was specifically required in view of a detectors vertical placement around a squared cavity [16]. The scintillation response to γ-rays and neutrons, in terms of light production per incident particle and as a function of its energy, is determined and theoretical response functions are validated by results of experiments performed in quasi-monoenergetic γ-ray and neutron fields.

2. Experimental set-up and data acquisition

The EJ-309 liquid scintillator that was characterized in this work was manufactured by Scionix. Its technical details are shown in Fig. 1. The detector consists of a cubic cell with 10 cm width, which is coupled to a 7.6 cm diameter photomultiplier tube (PMT, ETL type 9821 FLB) by a glass optical window made out of pyrex. The optical window penetrates inside the liquid volume to guarantee its complete contact with the liquid for every angular position of the detector cell. The penetration length of 9 mm was verified by a γ-ray radiography. The radiography also revealed the presence of an expansion void of approximately 5.4% of the liquid volume in the cell. This expansion volume is used to avoid damage caused by temperature variations.

The PMT was powered with a portable high voltage supply, model Canberra 3106D. No external light source was used for stabilizing the gain of the detector system. The optimum operating voltage was derived from a study of the detector response to radionuclide γ-ray sources, as discussed in Section 5.1. The best linearity and resolution was observed at -1250 V.

The anode output of the PMT was directly connected to a CAEN DT5751 digitizer [21], running the Digital Pulse Processing – Pulse Shape Discrimination (DPP-PSD) firmware for the acquisition and pre-processing of the pulses. The digitizer has a 10 bit resolution and was used with a sampling frequency of 1 GS/s. The effective number of bits (ENOB) is 9.04 [22]. Applying the interleaved operating mode which provides a sampling frequency of 2 GS/s would not have improved the pulse shape discrimination figure of merit (defined later) [23,22]. The acquired samples are integrated over time, eliminating the need for a charge sensitive preamplifier. A complete description of the digitizer acquisition algorithm can be found in Ref. [24]. The signal acquisition logic is illustrated in Fig. 2.

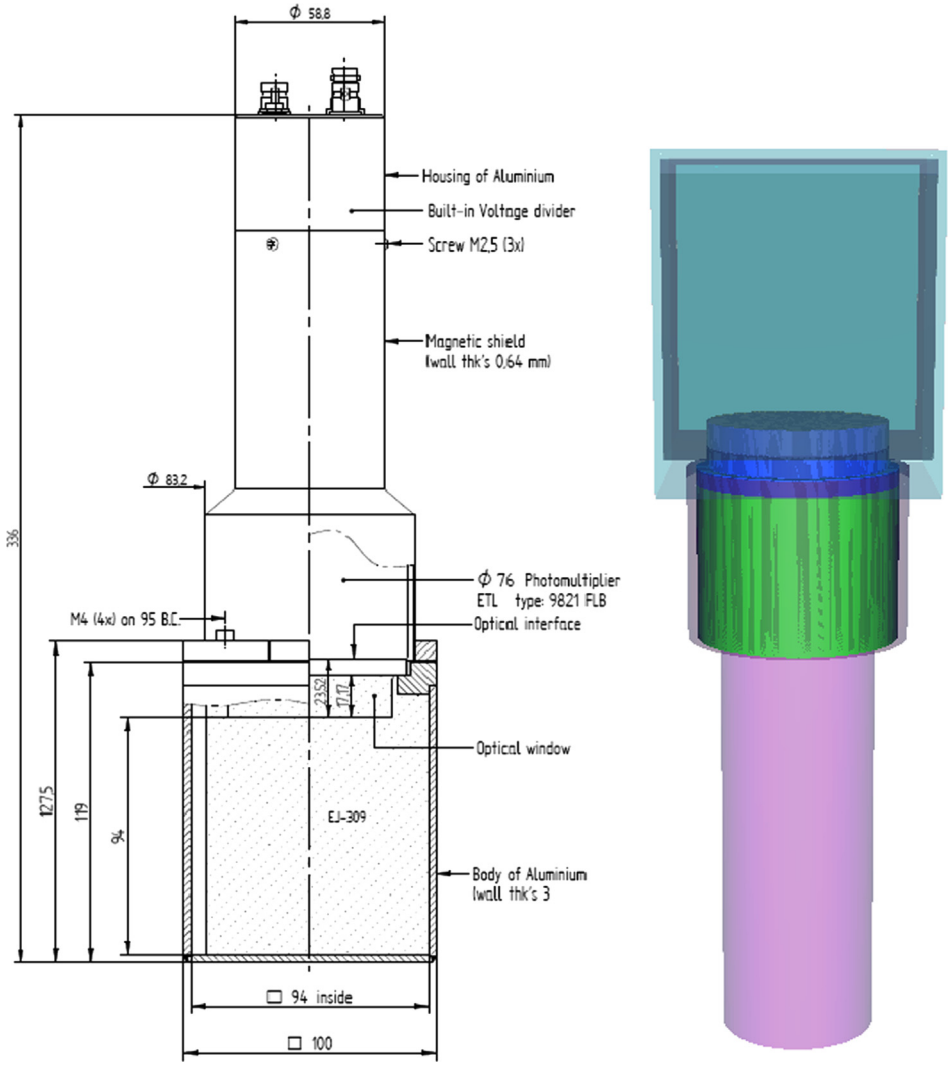

Fig. 1. Technical specification (left) of the EJ-309 liquid scintillator that was characterized in this work. The geometry modelled for the Monte Carlo simulations (right) is also shown.

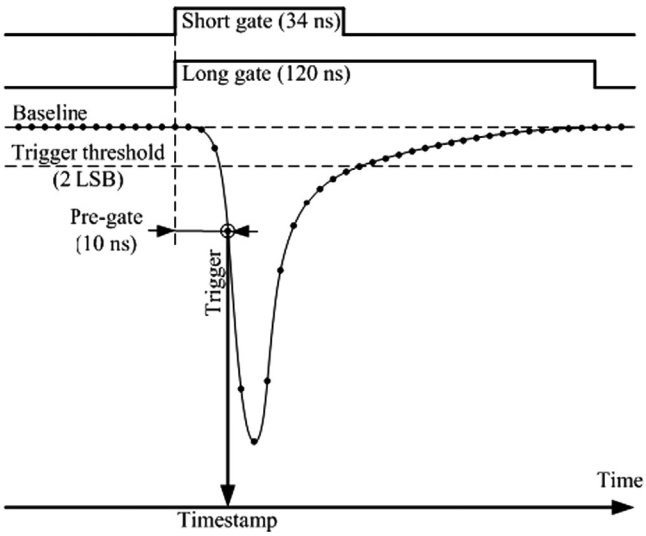

Fig. 2. Representation of the signal acquisition logic in the DPP-PSD firmware of the CAEN module [24].

A trigger level on the leading edge of the pulse initiates the processing of the acquired sample. This level, which reflects the minimum detectable light output, is set to avoid useless data processing of noise signals. The signal baseline is calculated by a moving average over a programmable number of samples acquired before the trigger. When a trigger occurs, the system opens two gates with different programmable widths. The gate lengths are set to account separately for the fast component of the pulse alone (short gate, τ_S) and to include also the slow component or pulse tail (long gate, τ_L). Integration of the voltage samples over these gates widths results in two values for the integrated charge, which are denoted by Q_S and Q_L for the short and long gate, respectively. A programmable pre-gate delay is used to open the gates before the trigger occurs. The settings of the trigger level, pre-gate delay and gate lengths are specified in Fig. 2.

In addition to the integrated charges, a time tag is produced which corresponds to the trigger time. In list mode operation, the firmware extracts the time tag together with the integrated charges Q_S and Q_L and transfers these values to a list mode output file. This file is subsequently post-processed using software developed at the JRC-IRMM to retrieve the PSD parameter, the time-difference between successive events and the time difference between a detected event and an external trigger. The latter is used for time-of-flight measurements with a pulsed beam. The software also includes the production of pulse height and time-of-flight spectra of the detected events. Hence, only the DPP part of the firmware of the CAEN module is used.

3. Pulse shape discrimination

The discrimination between events due to the detection of a γ-ray or a neutron is based on the shape of the fluorescence signals which are produced when charged particles are stopped in the detector [5,25]. The resulting scintillation pulse exhibits a fast rise time and a tail consisting of a fast and slow component. The fraction of the slow component increases with the stopping power of the charged particle and all principles of PSD are based on the different relative contribution to the slow component of pulses generated by particles with different mass. A pulse resulting from the detection of a neutron, which is mainly due to the production of light by protons, has a larger slow component compared to the one due to the detection of a γ-ray which results from light produced by electrons [5,25].

Various algorithms have been developed for discriminating events due to the detection of a neutron or γ-ray [5,26]. The most common one is the charge integration method, in which the pulse amplitude is integrated over two separate time intervals, accounting respectively for the fast and the slow (or the total) component of the pulse shape. A PSD parameter P_S is defined as [18,27]

$$P_S = 1 - \frac{Q_S}{Q_L} \tag{1}$$

where Q_L and Q_S are the above defined long and short gate integrated charges, respectively. The parameter P_S reflects the fraction of the light output due to the slow component. Other methods include a fit of the pulses with reference pulse shapes [28,29] or analytical functions [30,31]. They require the digitalization and acquisition of the whole pulse waveform, with limitations on the maximum data throughput of the experiments. For pulses with light outputs above 100 keV, the performances of the different algorithms are comparable.

The PSD algorithm applied in this work is based on the charge integration method. The optimum settings of the long and short gate were derived from results of measurements with an AmBe neutron source. For this measurements, the distance from the bare source to the detector was large enough to minimize the effect of pile-up, and no pulse rejection was performed on the acquired data. The histograms of the PSD parameter P_S resulting from measurements with different settings for τ_S and τ_L are shown in Fig. 3 and 4.

For each of these spectra a figure-of-merit was calculated [7]:

$$FOM = \frac{P_n - P_\gamma}{\Delta P_n + \Delta P_\gamma} \tag{2}$$

where P_n and P_γ are the PSD parameters corresponding to the peak in the spectrum resulting from the detection of neutrons and γ-rays, respectively, and ΔP_n and ΔP_γ their full widths at half maximum. The best PSD performance based on this figure of merit was obtained for $\tau_S = 34$ and $\tau_L = 120$ ns. Fig. 5 is a two dimensional representation of the PSD performance resulting from a measurement with an AmBe neutron source. The parameter P_S is plotted on the y-axis against the total light output. The colorbar indicates the number of detected events. Events resulting from the

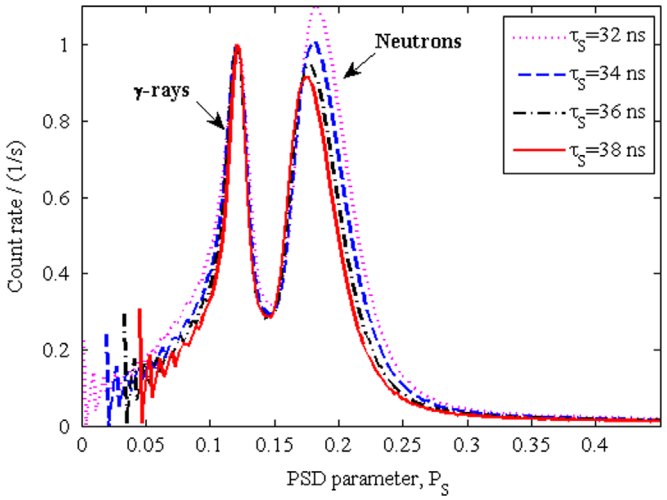

Fig. 3. Histograms of the PSD parameter P_S resulting from measurements with an AmBe source. The measurements were performed with a fixed $\tau_L = 80$ ns and variable τ_S. The histograms are normalized at the peak resulting from the detection of γ-ray events at $P_S = 0.12$. The data were taken with a fixed lower threshold of 200 keV on the light output.

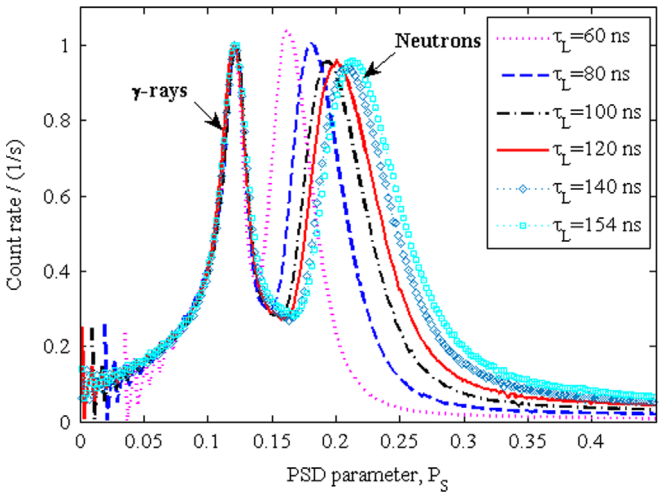

Fig. 4. Histograms of the PSD parameter P_S resulting from measurements with an AmBe source. The measurements were performed with a fixed τ_S=34 ns and variable τ_L. The histograms are normalized at the peak resulting from the detection of γ-ray events at P_S=0.12. The data were taken with a fixed lower threshold of 200 keV on the light output.

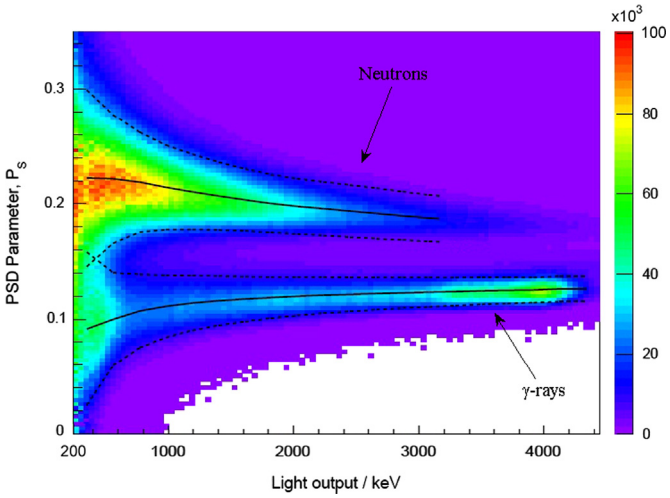

Fig. 5. Two dimensional representation of the distribution of the total light output L (in energy scale) and the PSD parameter P_S. The data result from measurements with an AmBe neutron source with τ_S=34 ns and τ_L=120 ns. The data are represented with a lower threshold of 200 keV on the light output. (For interpretation of the references to color in this figure caption, the reader is referred to the web version of this article.)

detection of a neutron or γ-ray are observed as two distinct clouds, which are centred around P_S=0.20 and P_S=0.12, respectively. At low energies the clouds start to overlap and a separation between γ-ray and neutron events becomes difficult. Hence, the figure of merit strongly depends on the threshold that is set on the total light output. This is illustrated in Fig. 6, where the FOM derived from the data in Fig. 5 is plotted as a function of the total light output. The FOM was obtained by fitting the histogram of the parameter P_S for a fixed light output by a sum of two Gaussian distributions. The resulting position and widths of the distributions have been used to indicate in Fig. 5 the events corresponding resulting from the detection of a neutron or γ-ray.

In this work, the events associated with the detection of a γ-ray were identified by $0.0 < P_S < 0.17$, whereas the events associated with the detection of a neutron were identified by $0.17 < P_S < 0.45$. The value P_S=0.17 represents the lower edge of the neutron cloud, as shown in Fig. 5.

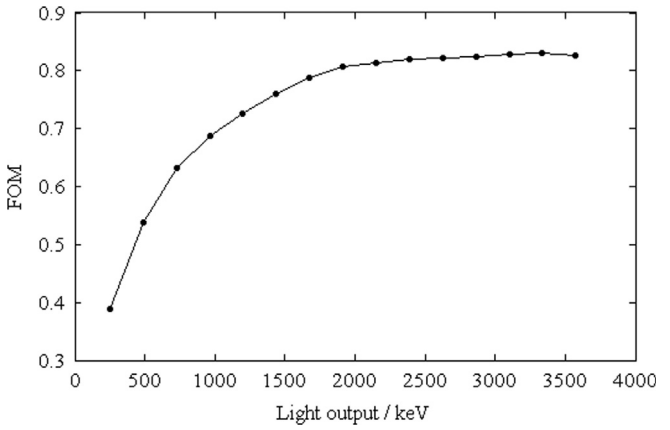

Fig. 6. FOM derived from the data in Fig. 5 as a function of the total light output. For the calculation of the FOM, the data in Fig. 5 were binned over intervals of 240 keV.

4. Theoretical response function

The response function $R(L,E)$ of a scintillation detector (or spectrometer) reflects the probability that after the detection of a γ-ray or neutron with energy E a light-output L is produced. This response function can be considered as a combination of a function $R_1(E_{cp},E)$, describing the energy E_{cp} that in the scintillator is transmitted to the charged particle by a γ-ray or neutron with energy E, and a function $R_2(L,E_{cp})$ expressing the probability that a charged particle with energy E_{cp} produces a light pulse with an amplitude L.

The response R_1 depends on the γ-ray or neutron transport in the detector material and can be determined with Monte Carlo simulations. The accuracy of such calculations relies on the quality of the nuclear data and on how well the details of the detector are known and included in the simulation input file. The function R_2 can be parametrized with a Gaussian distribution [32]:

$$R_2(L,E_{cp}) = \frac{1}{\sqrt{2\pi\sigma_L^2}} \cdot \exp\left(\frac{-(L-f(E_{cp}))^2}{2\sigma_L^2}\right) \quad (3)$$

where the light output function $f(E_{cp})$ and resolution function σ_L^2 depend on the energy E_{cp}.

Both the light output and resolution function are characteristic for each individual detector type and geometry [33]. They cannot be predicted and have to be determined by experiment [7,33]. Light output functions have been extensively studied for a variety of scintillators of different type and size [9,33–37]. They strongly depend on the charged particle type creating the light pulse [7,34,35]. For the majority of scintillators, the light output produced by electrons L_e is a linear function of the electron energy in the energy range between 0.04 MeV and 1.6 MeV [32,38,39], such that the observed integrated charge Q_L can be related to the electron energy E_e and the light output L_e by

$$Q_L = Q_0 + G_e L_e = Q_0 + G_e(E_e - E_0) \quad (4)$$

where E_0, which is mostly taken to be 5 keV, accounts for quenching effects in the scintillator at small energies [32,40]. The calibration factor G_e is used to transfer the observed integrated charge, which is recorded in channels, into an electron equivalent light output L expressed in energy units [32]. The parameter Q_0 in Eq. (4) accounts for a possible offset due to the electronics. The G_e factor together with the offset Q_0 is derived by comparing experimental and theoretical response functions for a set of γ-rays as described in Section 5.1. At higher energies deviations from the linear dependence of the light output as a function of electron energy have been reported by Refs. [37,39,41].

The light output produced by charged particles heavier than the electron is known to be non-linear [9]. Various parametric formulae have been proposed to describe them, ranging from a semi-empirical approach based on the specific energy loss [25,34–37,42,43] to full empirical analytical expressions as a function of the charged particle energy [44,45,37]. The formulae used by Madey et al. [44]:

$$L_p = a_0 E_p + a_1 (1 - e^{-a_2 E_p^{a_3}}) E_p \tag{5}$$

and Kornilov et al. [37]:

$$L_p = \frac{b_1 E_p}{1 + b_2 E_p} E_p, \tag{6}$$

seem to be good approximations to describe the non-linear behavior of the light output produced by protons for a variety of scintillators [37,46–49], including EJ-309 liquid scintillators [19]. Eq. (6) has also been used by Kornilov et al. [37] to account for the non-linear electron light output.

The resolution function σ_L^2 is mostly parametrized by [7,32,50,51]

$$\sigma_L^2 = \alpha^2 L^2 + \beta^2 L + \gamma^2 \tag{7}$$

and expresses the independent contributions due to the position-dependent light transmission from the scintillator to the photo-cathode (α), the statistical nature of the light production and amplification (β), and the electronic noise (γ). The value of the parameter α limits the resolution of the detector at large light outputs, while the contribution of the noise can mostly be neglected. The parameter α depends strongly on the geometry and can be estimated theoretically [50].

The resolution function depends on the properties of the detector components and its construction details [38]. However, the function does not strongly depend on the particle type producing the light, as demonstrated in Refs. [37,38]. Therefore, the parameters α, β and γ can be determined from measurements with γ-ray radionuclide sources.

Assuming multiple interaction events can be neglected, the response function $R(L, E)$ can be approximated by the convolution of the response functions R_1 and R_2:

$$R(L, E) = \int R_1(E_{cp}, E) \cdot R_2(L, E_{cp}) \cdot dE_{cp}. \tag{8}$$

When these conditions are not fulfilled, e.g. for large volume scintillators, the calculation of the response function $R(L, E)$ requires a Monte Carlo simulation accounting for the full processes of particle transport and light production.

In this work, theoretical response functions are derived from Monte Carlo simulations based on a combination of two codes: a particle transport code simulating the tracks of neutrons and γ-rays in the scintillation material and the transfer of energy to the charged particles by multiple collisions, and a post-processor accounting for the light production by the charged particles. The particle transport simulations were performed with the MCNPX-PoliMi code [52]. This code is specifically tailored at the simulation of detector responses when the separate treatment of each particle interaction occurring within the detection material is required. The code provides a list mode file reporting single interaction information on user-selected portions of the system geometry, e.g. the detector cell. The detector geometry and materials, as well as the experimental conditions of the measurements, were carefully reproduced in the simulations to reduce bias effects in the calculation of the response function. Fig. 1 shows the modelled geometry of the detector cell.

The output file from the MCNPX-PoliMi code is treated by the SimPLiS code (Simulation Post-processor for Liquid-Scintillators), which accounts for the light production and produces the full response function $R(L, E)$. The SimPLiS post-processor code is a sub-part of the SimPLiS-NCC code [53], which was developed at the JRC-ITU (Ispra) for a particular safeguards application using a set of EJ-309 detector cells [16]. Depending on the incident particle type and target atom, the energy transmitted in each collision is converted into scintillation light using the parametrized light output and resolution functions of the detector. The simulation of the photon transport to the photo-cathode is not performed but the light production, including resolution broadening, is calculated by sampling the produced light over a Gaussian probability distribution whose mean is defined by the light output function and its standard deviation is defined by the resolution parameters (α, β and γ). The total light output $L = \sum_{i=1}^{n} L_i$ is derived by summing up the light $L_{i=1,\ldots,n}$ produced in subsequent collisions occurring within a specified time window, which is defined by the rise time of the pulse. In case of multiple collisions, the variance of the Gaussian distribution for a pulse of total light output L becomes:

$$\sigma_L^2 = \alpha^2 \sum_{i=1}^{n} L_i^2 + \beta^2 L + \gamma^2. \tag{9}$$

5. Experimental response function

To calculate theoretical response functions, the calibration parameters (Q_0, G_e) and the light output and resolution functions are required. They have been determined from measurements in quasi-monoenergetic γ-ray and neutron fields carried out at the EC-JRC-IRMM in Geel and at the PTB Ion Accelerator Facility (PIAF) of the PTB in Braunschweig [54], following the procedures described in Ref. [33]. The parameters in the analytical function in Eqs. (4)–(6) were derived from a least squares adjustment to experimental response functions using the theoretical ones discussed in Section 4. The final response functions for neutrons were validated with measurements with an AmBe source. For all these experiments the detector with PMT was positioned vertically as illustrated in Fig. 7.

5.1. Response functions for γ-rays

Experimental response functions for γ-rays were obtained from measurements with a set of radionuclide γ-ray sources, which were placed at 45.5 cm from the detector face. The characteristics of the sources are reported in Table 1.

The experimental response functions obtained from measurements with a ^{137}Cs and ^{207}Bi source, shown in Fig. 8, illustrate that the interaction of γ-rays with the scintillating material occurs mainly by means of Compton scattering with electrons. Background measurements were performed regularly during the experimental campaign and the background contribution was subtracted. These histograms were used to derive the calibration factor G'_e, with $Q_L = G'_e\,(E_e - E_0)$, and resolution parameter α'^2, with

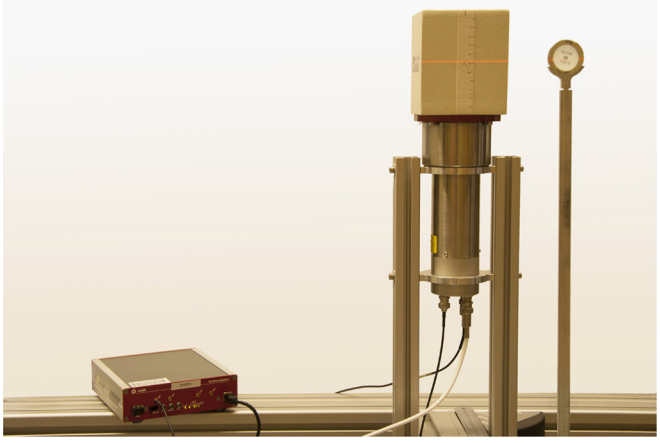

Fig. 7. Detector setup for γ-ray measurements.

$\sigma_L^2 = \alpha'^2 L^2$, from a fit to the data in the region of the Compton edge. This procedure was performed for the spectra resulting from both the long and short gates. The calibration factor G'_e as function of the Compton energy, shown in Fig. 9, reveals that the observed integrated charge derived from the long gate is in first approximation directly proportional to the electron energy and no offset correction is required, i.e. $Q_0=0$. The increase of G'_e with energy for electron energies below 1500 keV, which was confirmed by repeated measurements with a ^{137}Cs and ^{207}Bi source, is not understood and requires further investigation. Similar conclusions can be drawn for the data resulting from the short gate. From the data in Fig. 9 an average calibration factor G_e was derived to convert the observed charge into an electron equivalent light expressed in units of energy. The ratio of the average calibration factors for the short gate and long gate, confirms that 85% of the light that is produced by electrons results from the fast component.

The relative resolution as a function of light output in Fig. 10 can be approximated by Eq. (7). The parameters ($\alpha^2=0.0016$, $\beta^2=1.42$, $\gamma^2=25$) have been determined from a fit to the data points. The result is represented by the full line in Fig. 10.

Additionally, the experimental light output histograms were used to derive the expected activity of the source A_{exp} by a fit of the theoretical response functions in the regions of the Compton edges. The data in Table 2 reveal that the activity derived from a fit to the light output histograms is in very good agreement with the declared activity. This indicates that the detector details, including the effective volume of the liquid, the stoichiometry of the liquid and the expansion volume, are well reproduced in the geometry input file and the absolute detection efficiency can be predicted within 2%.

Theoretical response functions have been calculated using the calibration factor G_e and resolution parameters (α, β and γ). Fig. 8 reveals the good agreement between the experimental and theoretical response functions for γ-rays. It should be noted that the calculated responses were based on the declared activities of the sources and the calculated data were not scaled to match the experimental results.

Table 1
Characteristics of the radionuclide sources used to determine the light output and resolution functions for electrons. The declared activity A_d is given together with the energy E_γ of the most intense γ-rays and the corresponding energy of the Compton edge (E_C).

Source	$T_{1/2}$ / y	A_d/kBq	E_γ /keV	E_C / keV	Ref.
^{137}Cs	30.05	21.98	662	477	[55]
^{60}Co	5.27	11.60	1173	950	[55]
			1332	1104	[55]
^{207}Bi	32.90	30.70	570	394	[55]
			1064	858	[55]
			1770	1547	[55]
^{208}Tl (from ^{232}Th)	1.4×10^{10}	N.A.	2614	2382	[55]
AmBe	432.60	N.A.	4443	4201	[56]
PuC	87.74	N.A.	6130	5885	[57]

5.2. Response functions for neutrons

5.2.1. Experimental conditions

The 3.75 MV Van de Graaff (VdG) accelerator of PTB was used to produce quasi-monoenergetic neutron beams in the energy region between 300 keV and 2.7 MeV. Pulsed deuteron beams produced at the cyclotron were used to study response functions for neutron energies between 2.5 MeV and 14 MeV. Measurements with a ^{137}Cs and ^{207}Bi source were carried out before and after the measurements at the neutron beams to calibrate the pulse height spectra in energy.

At the VdG facility quasi-monogenergetic neutron beams were produced by the ^{7}Li(p,n)^{7}Be and the T(p, n)^{3}He reactions [58]. The measurements with the LiF target, with an areal density of 37 μg cm^{-2}, were carried out with proton beam energies between 2.05 MeV and 2.9 MeV, resulting in quasi-monoenergetic neutron beams between 300 keV and 1.2 MeV, respectively. For the measurements with the T/Ti target, with an areal density of 853 μg cm^{-2} and T/Ti number ratio of 1, the proton beam energy was varied between 1.7 MeV and 3.5 MeV, leading to neutrons beams between 0.8 MeV and 2.7 MeV, respectively. The detector

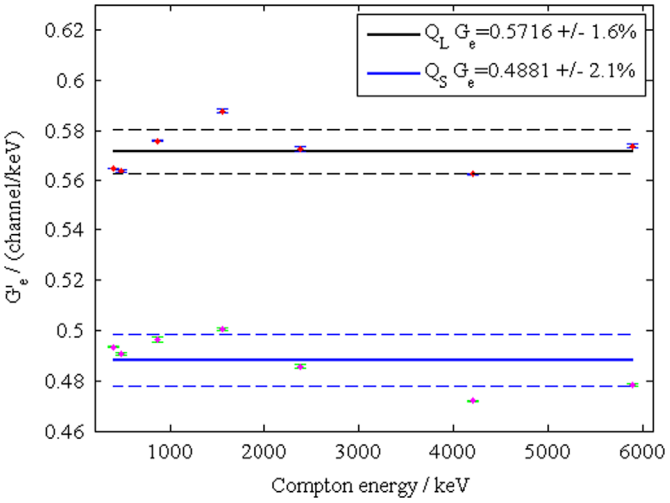

Fig. 9. Calibration factors G'_e as a function of the Compton energy. The full line represents the average calibration factor G_e of the detector.

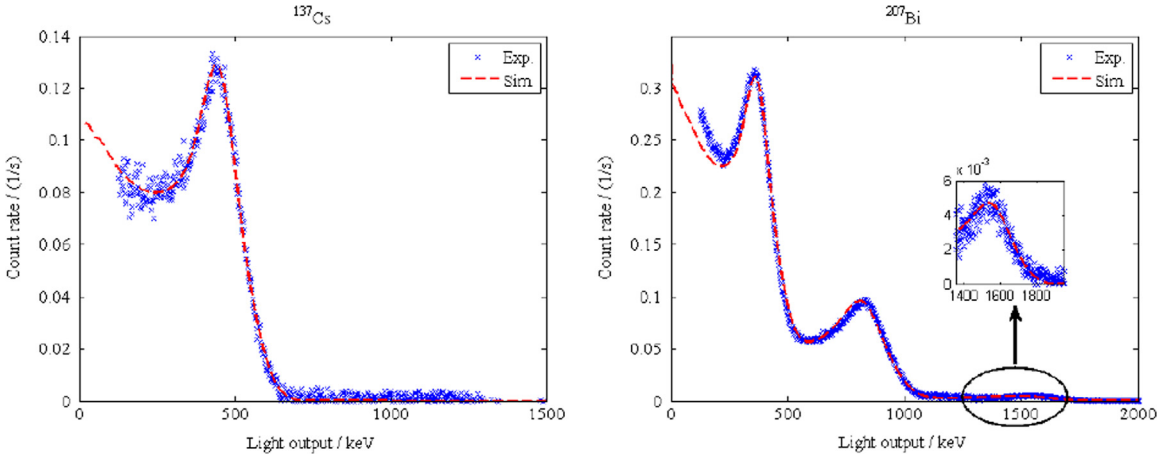

Fig. 8. Experimental and theoretical response functions obtained from measurements with a ^{137}Cs (left) and a ^{207}Bi (right) γ-ray sources.

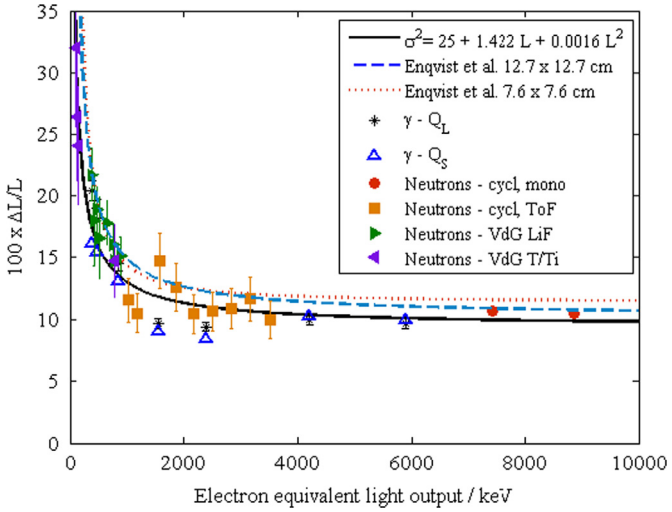

Fig. 10. The relative resolution $\Delta L/L$, with ΔL expressed in FWHM, as a function of the light output L. The data resulting from measurements with the γ-ray sources are represented by an asterisk (*) for the long and by a triangle (Δ) for short gate. The data derived from the response functions for neutrons are represented by open circles (o) for the cyclotron monoenergetic peaks, by squares (□) for the time-of-flight data, by right pointed triangles (▷) for the VdG data with the LiF target and by left-pointed triangles (◁) for the VdG data with the T/Ti target. The full line is the result of a least squares fit using the neutron data and the γ-rays data points for the long gate. The results are compared with those obtained by Enqvist et al. [19] for two cylindrical EJ-309 liquid scintillators.

Table 2
Ratio of the activity A_{exp}, derived from the experimental response, and the declared activities A_d for three γ-ray sources. The experimental activity was obtained from a least-squares fit in the region of the Compton edge. The uncertainties result from a propagation of only the counting statistics uncertainty.

Source	A_d/kBq (%)	$\frac{A_{exp}}{A_d}$
^{137}Cs	21.98 ± 1.0	1.010 ± 0.003
^{60}Co	11.60 ± 0.7	1.020 ± 0.003
^{207}Bi	30.70 ± 3.0	1.000 ± 0.012

was placed at a 4.03 m distance from the target and at 0° with respect to the proton beam axis. The background contribution due to scattered neutrons was determined by measurements with a shadow cone consisting of iron (200 mm, thin side) and polyethylene (200 mm, thick side). The small and large diameters are 32 mm and 52 mm, respectively. The cone was placed at 45 cm distance from the target, creating a shadow of 20 cm diameter at the detector position.

At the cyclotron neutron beams were produced by accelerating a pulsed deuteron ion beam into a deuterium gas target. The cyclotron was operated with a main frequency of approximately 13 MHz. Due to the limitations in the CAEN software used during the experiments presented in this work, the digitizer system was not able to handle count rates above 96 kHz. Therefore, the effective frequency of the charged particle beam hitting the target was reduced to 57 kHz by a beam pulse selector. Measurements were performed for a 9.14 MeV and 11.06 MeV deuteron beam, resulting in mono-energetic peaks for the main reaction of 12.21 and 14.03 MeV respectively. The spectrum is dominated by mono-energetic neutrons produced by the D(d,n)^{3}He reaction. The continuum spectra, resulting from the D(d,np)D and D(d,n)n2p break up reactions, in combination with time-of-flight measurements were used to study response functions in the energy region between 2.5 MeV and 7.5 MeV. The detector was placed at 20.697 m from the target. For each deuteron energy complementary measurements with an empty target chamber were carried out to account for ambient background neutrons and neutrons resulting from beam interactions in the accelerator and the target structure. To perform time-of-flight measurements a start signal derived from the pulsed ion beam was sent as an additional input signal to the CAEN digitizer. The TOF-spectra with and without gas in the target chamber resulting from measurements with a 11.06 MeV deuteron beam are compared in Fig. 11. The position of the peak resulting from the detection of γ-rays was used to derive the zero point of the TOF scale. The peak in Fig. 11 at 400 ns is due to mono-energetic neutrons with an energy of 14.03 MeV produced in the D(d,n)^{3}He reaction. The other peaks in the spectrum are satellite peaks which result from spurious deuteron beam pulses produced in the main frequency of the cyclotron that were not removed from the beam by the beam selector. Additional light output spectra for fixed neutron energies were derived by selecting events with fixed TOF values. The TOF-bin width corresponded to an energy width of about 5%, which is a factor 2 lower than the resolution at the highest energies encountered. Examples of such spectra are shown in Fig. 12.

5.2.2. *Light output and resolution functions*

The spectra in Fig. 12 were used to derive the light output and resolution functions for protons. For each spectrum a parameter $R_p = L/E_p$ and resolution parameter $\alpha'^2 = \sigma_L^2/L^2$ was derived, with E_p the energy of the proton producing the light. For the spectra obtained at the VdG the energy distribution of the neutrons was taken into account in the calculation of the theoretical response. This distribution was calculated by the EnergySet [59] and NeuSDesc [60] codes developed at the EC-JRC-IRMM. EnergySet calculates neutron energy spectra and fluencies for quasi-monoenergetic neutron fields produced by charged particle induced reactions. It uses the stopping powers from Refs. [61,62], the differential cross-sections from Refs. [63,64] and kinematics to calculate the neutron spectrum as a function of the ion beam energy and current, target thickness, neutron emission angle and detector distance. For LiF targets, the competing reaction ^{7}Li(p,n)^{7}Be*, which generates a lower energy neutron peak, is included in the calculation of the total neutron flux distribution. NeuSDesc is an extended version of EnergySet. It also accounts for broadening due to energy and angular straggling of the ion beam and non-homogeneities of the entrance foil for gas targets. To simulate the stopping of the ion beam in the target the SRIM-2008 code [65] is used.

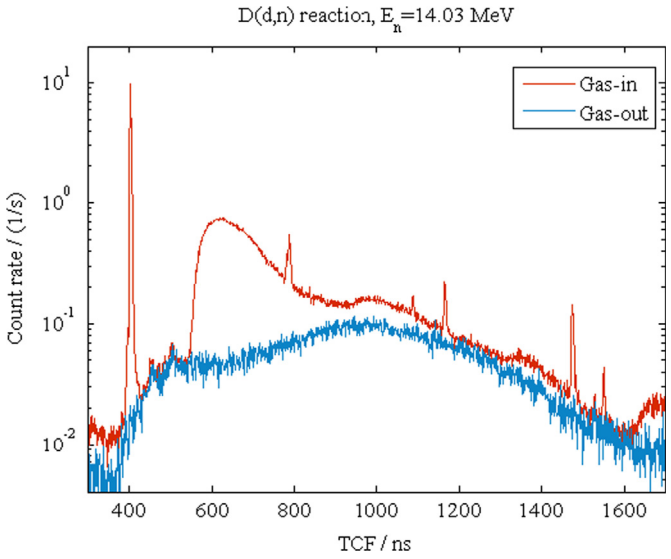

Fig. 11. Gas-in and gas-out neutron TOF spectra for a cyclotron measurement with a deuteron beam of 11.06 MeV.

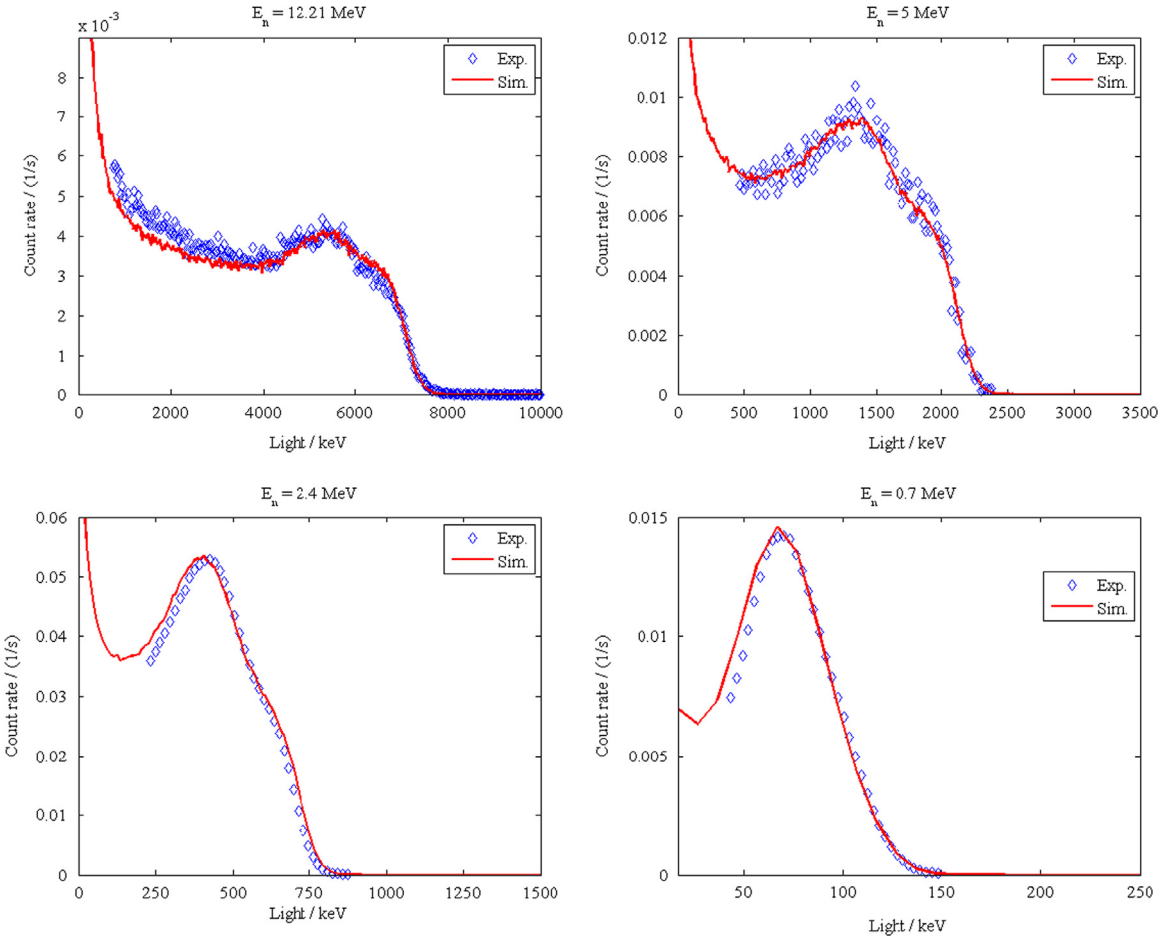

Fig. 12. Examples of experimental and theoretical response functions obtained by mono-energetic peak (top left) and time-of-flight (top right) measurements at the PTB cyclotron with a deuteron beam, and by neutron measurements with the LiF target (bottom left) and the T/Ti target (bottom right) at the VdG accelerator.

The light output for protons in the EJ-309 cell can be approximated by Eq. (5) and by a modified version of the function proposed by Kornilov et al. [37]:

$$L_p = b_0 E_p + \frac{b_1 E_p}{1 + b_2 E_p} E_p. \tag{10}$$

Using Eqs. (5) and (10) the experimental data are reproduced within 0.8% and 1%, respectively, at the 1 sigma level, with the parameters (a_0=0.80, a_1=−2519, a_2=3.68 × 10^{-4} and a_3=0.96) for Eq. (5) and (b_0=0.082, b_1=1.36 × 10^{-4} and b_2=1.80 × 10^{-4}) for Eq. (10). The parameters are obtained from a least squares adjustment to the data. Without including the term b_0, i.e. using the formula proposed by Kornilov et al. [37], the deviation between fitted and experimental data is 2%.

The influence of multiple interaction events is illustrated in Fig. 13 for the response to 5 MeV neutrons. Since the response is dominated by the multiple interaction events, the quality of the simulated response strongly depends on how well the non-linear behavior of the light output function is known.

Fig. 14 shows that the light output function for protons for the EJ-309 detector studied in this work is very close to the general function that is derived at PTB from a study of several organic liquid scintillators of different geometry and size [66]. The energy dependence of the specific light output for the EJ-309 detector studied in this work is similar to the one reported by Enqvist et al. [19] for a cylindrical EJ-309 cell with dimensions (12.7 cm × 12.7 cm). However, the light output reported for this detector with a 60% larger volume is systematically lower. The light output derived by Enqvist et al. [19] for a cylindrical EJ-309 cell with a smaller volume (7.6 cm × 7.6 cm) is also different from the rectangular cell studied in this work and the larger cell studied by Enqvist et al. [19]. It should be noted that the light output functions of Enqvist et al. [19] were derived from experimental response functions up to 6 MeV neutron deposited energy.

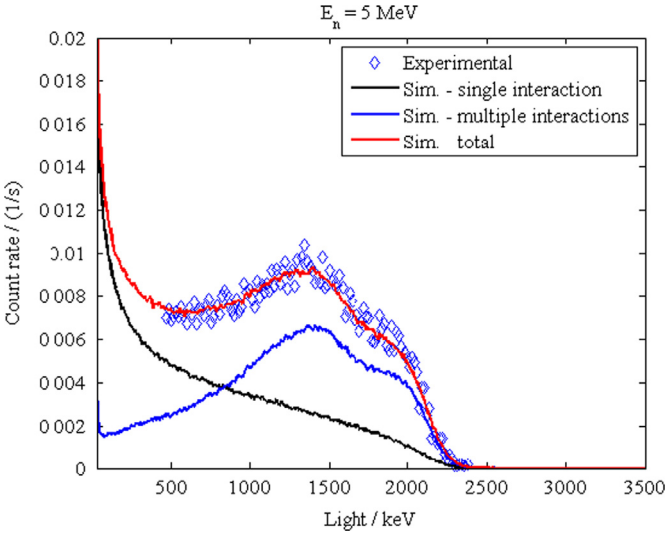

Fig. 13. Contribution of single and multiple interaction events to the total response of the EJ-309 detector presented in this work for 5 MeV neutron energy. The experimental response was obtained from TOF-measurements at the PTB cyclotron.

The data in Fig. 10 reveal that the relative resolution for light produced by protons is similar to the one for light produced by electrons. The resolution of the detector characterized in this work is slightly better compared to two cylindrical EJ-309 detectors of similar sizes studied in Ref. [19], as illustrated in Fig. 10.

5.3. Measurements with an AmBe(α,n) source

Measurements with an AmBe(α,n) neutron source were performed at the EC-JRC-IRMM in the same experimental conditions as those for the γ-ray measurements described in Section 5.1. Measurements with a ^{137}Cs source were regularly performed to control the stability of the detection system. During the 10 days of measurement time, including the background run, a 1.5% drift in gain was observed, and the experimental data were corrected for the gain shift using the 4.44 MeV γ peak of the AmBe source. The neutron source was certified for its neutron output $(7.711 \pm 0.050) \times 10^4\ s^{-1}$ by measurements in a manganese bath. The resulting histogram of the electron equivalent light output for events resulting from the detection of a neutron is shown in Fig. 15. The data were only corrected for ambient background radiation. No shadow cone measurements were performed to correct for room scattering.

The theoretical response function was calculated with Monte Carlo simulation using the simulation tools described in Section 4. For the simulations the AmBe(α,n) neutron spectrum recommended in the ISO standard was used [67]. Using the light output and resolution functions described in the previous section, the data in Fig. 15 were used to derive the neutron intensity of the source by a fit of the theoretical response to the measured data in the light output region with $1500\ keV < L < 6500\ keV$. The resulting intensity is $(8.00 \pm 0.01)\ 10^4\ s^{-1}$, where the quoted uncertainty is only due to counting statistics. An overall uncertainty of 4% is expected on the result and is mainly due to imperfect PSD separation between γ and neutron events, and background fluctuations which affect the measurements given the relatively weak strength of the AmBe source. Therefore, the above quoted value is consistent with the declared value. The good agreement between experimental and calculated response also confirms the light output for protons derived in this study.

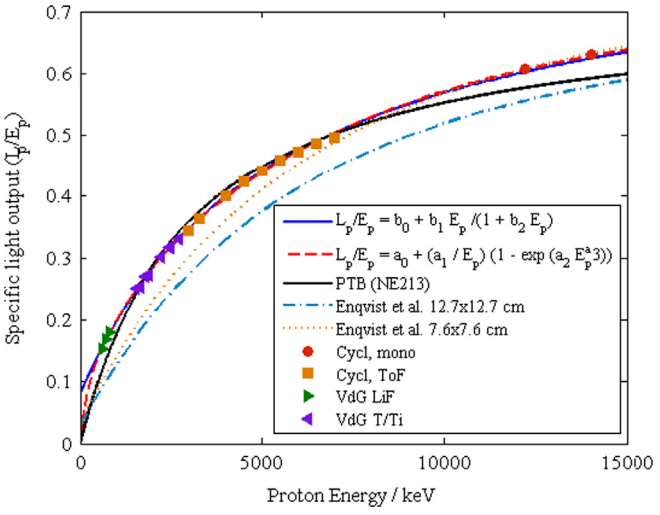

Fig. 14. Specific light output function for protons for the EJ-309 detector studied in this work. The data derived from the response functions for neutrons are represented by open circles (o) for the cyclotron monoenergetic peaks, by squares (□) for the time-of-flight data, by right pointed triangles (▷) for the VdG data with the LiF target and by left-pointed triangles (◁) for the VdG data with the T/Ti target. The full and dashed lines are the result of a least squares fit using Eqs. (5) and (10) respectively. The results are compared with those obtained by Enqvist et al. [19] for two cylindrical EJ-309 liquid scintillators, and by PTB [66].

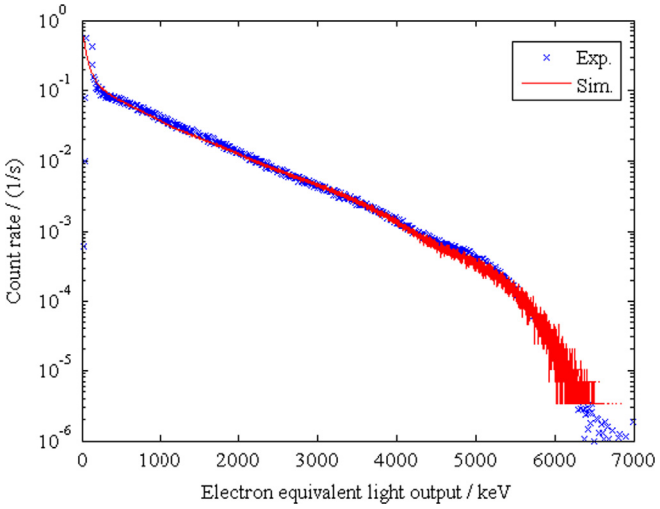

Fig. 15. Experimental and simulated pulse height spectra obtained from measurements with an AmBe neutron source. The light output and resolution functions used for the computation of the simulated response are discussed in Section 5.2.2.

6. Summary

In this work a characterization of a cubic EJ-309 liquid scintillator detector of 10 cm width is presented. The detector was characterized for its response to γ-rays and neutrons by means of calibrated radionuclide γ-ray sources in the energy range from 400 keV to 6 MeV, and by quasi-monoenergetic neutron beams at the PTB Van der Graaff accelerator in the energy range from 500 keV to 2.7 MeV, and time-of-flight measurements at the PTB cyclotron in the range from 2.5 to 14 MeV. The results of the γ-ray measurements were used to verify the detection efficiency for γ-rays and the linearity and resolution of the detector in the set experimental conditions. The detection efficiency for γ-rays resulting from the simulations were confirmed within 2%. The light output and resolution functions for electrons and protons were derived by a least squares adjustment to experimental data using theoretical response functions determined by Monte Carlo simulations and a post-processing code to account for multiple interaction events in the detector. The derived resolution function and light output for neutron were compared to those found in the literature for similar liquid scintillator detectors of different geometries. The comparison revealed how the detector characterized in this work exhibits a similar behavior as compared to other liquids. However, on an absolute scale differences are observed even for cells filled with the same liquid (EJ-309). Hence, the need for a separate experimental characterization of cells of different geometries and using different PMTs is again evidenced.

The simulated response function for neutron was validated by results of measurements with an AmBe neutron source. The detection efficiency for neutrons resulting from the simulations was confirmed within 4%.

The results presented in this work indicate that the cubic EJ-309 detector is suitable for use in mixed γ-ray and neutron fields. The derived light output and resolution functions combined with Monte Carlo simulations can be used to reproduce the full response matrix which can be used in various applications ranging from neutron and γ-ray spectrometry to nuclear safeguards and security.

Acknowledgments

This work was supported by the European Commission within the support programme to the IAEA, task EC-A-1362. The authors acknowledge the IAEA Department of Safeguards – Division for Scientific and Technical Services (SGTS) for having provided the detector cell. The authors thank the operators of the PTB Van de Graaff accelerator and cyclotron for providing the conditions necessary for these experiments. The authors also acknowledge the work of the anonymous referees for their valuable comments and suggestions which improved the original manuscript.

References

[1] A.S. Vorobyev, O.A. Shcherbakov, Y.S. Pleva, A.M. Gagarski, G.V. Val'ski, G.A. Petrov, V.I. Petrova, T.A. Zavarukhina, Nuclear Instruments and Methods in Physics Research Section A 598 (2009) 791.
[2] N. Kornilov, F.-J. Hambsch, I. Fabry, S. Oberstedt, T. Belgya, Z. Kis, L. Szentmiklósi, S. Simakov, Nuclear Science and Engineering 165 (2010) 117.
[3] S. Unholzer, H. Freiesleben, H. Klein, K. Seidel, Nuclear Instruments and Methods in Physics Research Section A 476 (2002) 160.
[4] Y.A. Kaschuck, B. Esposito, L.A. Trykov, V.P. Semenov, Nuclear Instruments and Methods in Physics Research Section A 476 (2002) 511.
[5] H. Klein, Radiation Protection Dosimetry 107 (2003) 125.
[6] F.D. Brooks, H. Klein, Nuclear Instruments and Methods in Physics Research Section A 476 (2002) 1.
[7] H. Klein, S. Neumann, Nuclear Instruments and Methods in Physics Research Section A 476 (2002) 132.
[8] D. Schmidt, H. Klein, Precise Time-of-Flight Spectrometry of Fast Neutrons – Principles, Methods and Results, Technical Report, Physikalisch-Technische Bundesanstalt (PTB); 1998.
[9] V.V. Verbinski, W.R. Burrus, T.A. Love, W. Zobel, N.W. Hill, Calibration of an organic scintillator for neutron spectrometry, Nuclear Instruments and Methods in Physics Research Section A 65 (1968) 8.
[10] H. Klein, Radiation Protection Dosimetry 107 (2003) 95.
[11] M. Matzke, Radiation Protection Dosimetry 107 (2003) 155.
[12] ELJEN Technology, EJ-309 URL ⟨http://www.eljentechnology.com/index.php/products/liquid-scintillators/73-ej-309⟩.
[13] M.D. Joyce, M.D. Aspinall, F.D. Cave, K. Georgopoulous, Z. Jarrah, IEEE Transactions on Nuclear Science NS-57 (5) (2010) 2625.
[14] M.D. Joyce, M.D. Aspinall, F.D. Cave, A.D. Lavietes, IEEE Transactions on Nuclear Science NS-59 (4) (2012) 1245.
[15] L. Stevanato, D. Cester, G. Nebbia, G. Viesti, Nuclear Instruments and Methods in Physics Research Section A 690 (2012) 96.
[16] A.D. Lavietes, R. Plenteda, N. Mascarenhas, L.M. Cronholm, M. Aspinall, M. Joyce, A. Tomanin, P. Peerani, Liquid scintillator-based neutron detector development, 01/2012, in Proceeding of the Nuclear Science Symposium and Medical Imaging Conference (NSS/MIC), 2012 IEEE. http://dx.doi.org/10.1109/NSSMIC.2012.6551100.
[17] J.L. Dolan, E.C. Miller, A. Enqvist, M. Flaska, A. Tomanin, P. Peerani, D.L. Chicester, S. Pozzi, Development of a passive neutron-multiplicity system based on organic scintillators for nuclear safeguards applications, Nuclear Instruments and Methods in Physics Research Section A, submitted for publication.
[18] I.A. Pawełczak, S.A. Ouedraogo, A.M. Glenn, R.E. Wurtz, L.F. Nakae, Nuclear Instruments and Methods in Physics Research Section A 711 (2013) 21.
[19] A. Enqvist, C.C. Lawrence, B.M. Wieger, S.A. Pozzi, T.N. Massey, Nuclear Instruments and Methods in Physics Research Section A 715 (2013) 79.
[20] A. Enqvist, K.J. Weinfurther, M. Flaska, S.A. Pozzi, IEEE Transactions on Nuclear Science 11 (2011) http://dx.doi.org/10.1109/TNS.2011.2164554.
[21] CAEN Electronic Instrumentation, DT5751 Technical Specifications. URL ⟨http://www.caen.it/csite/CaenProd.jsp?idmod=632&parent=14⟩.
[22] M. Flaska, M. Faisal, D.D. Wentzloff, S.A. Pozzi, Nuclear Instruments and Method in Physics Research Section A 729 (2013) 456.
[23] C. Hellesen, M. Skiba, G. Ericsson, E.A. Sundén, F. Binda, S. Conroy, J. Eriksson, M. Weiszflog, Nuclear Instruments and Method in Physics Research Section A 720 (2013) 135.
[24] CAEN Electronic Instrumentation, DPP-PSD Documentation. URL ⟨http://www.caen.it/csite/CaenProd.jsp?idmod=770&parent=39⟩.
[25] J.B. Birks, The Theory and Practice of Scintillation Counting, Pergamon Press, Oxford, 1964.
[26] G. Ranucci, A. Goretti, P. Lombardi, Nuclear Instruments and Methods in Physics Research Section A 412 (1998) 374.
[27] B. Esposito, Y. Kaschuck, A. Rizzo, L. Bertalot, A. Pensa, Nuclear Instruments and Methods in Physics Research Section A 518 (2004) 626.
[28] C. Guerrero, D. Cano-Ott, M. Fernández-Ordónez, E. González-Romero, T. Martínez, D. Villamarín, Nuclear Instruments and Methods in Physics Research Section A 597 (2008) 212.
[29] S.D. Ambers, L. Huang, M. Flaska, S.A. Pozzi, Template-matching neutron/gamma-ray pulse shape discrimination, in: Proceedings of the 51st INMM Annual Meeting, INMM, Article 476, 2010.
[30] G. Ranucci, Nuclear Instruments and Methods in Physics Research Section A 354 (1995) 389.
[31] S. Marrone, D. Cano-Ott, N. Colonna, C. Domingo, F. Gramegna, E.M. Gonzalez, F. Gunsing, M. Heil, F. Käppeler, P.F. Mastinu, P.M. Milazzo, T. Papaevangelou, P. Pavlopoulos, R. Plag, R. Reifarth, G. Tagliente, J.L. Tain, K. Wisshak, Nuclear Instruments and Methods in Physics Research Section A 490 (2002) 299.
[32] G. Dietze, Energy calibration of NE-213 scintillation counters by γ-rays, IEEE Transactions on Nuclear Science NS-26 (1) (1979).
[33] D. Schmidt, B. Asselineau, R. Böttger, H. Klein, L. Lebreton, S. Neumann, R. Nolte, G. Pichenot, Nuclear Instruments and Methods in Physics Research Section A 476 (2002) 186.
[34] R. Batchelor, W.B. Gilboy, J.B. Parker, J.H. Towle, Nuclear Instruments and Methods in Physics Research Section A 13 (1961) 70.
[35] R.L. Craun, D.L. Smith, Nuclear Instruments and Methods in Physics Research Section A 80 (1970) 239.
[36] S. Mouatassim, G.J. Costa, G. Guillaume, B. Heusch, A. Huck, M. Moszyński, Nuclear Instruments and Methods in Physics Research Section A 359 (1995) 530.
[37] N.V. Kornilov, I. Fabry, S. Oberstedt, F.-J. Hambsch, Nuclear Instruments and Methods in Physics Research Section A 599 (2009) 226.
[38] G. Dietze, H. Klein, Nuclear Instruments and Methods in Physics Research Section A 193 (1982) 549.
[39] T. Novotny, L. Büermann, S. Guldbakke, H. Klein, Nuclear Instruments and Methods in Physics Research Section A 400 (1997) 356.
[40] F.T. Porter, M.S. Freedman, F. Wagner Jr., I.S. Sherman, Nuclear Instruments and Methods in Physics Research Section A 39 (1966) 35.
[41] L. Büermann, S. Ding, S. Guldbakke, H. Klein, T. Novotny, M. Tichy, Nuclear Instruments and Methods in Physics Research Section A 332 (1993) 483.
[42] C.N. Chou, Physical Review 87 (1952) 904.
[43] G.T. Wright, Physical Review 91 (1953) 1282.
[44] R. Madey, F.M. Waterman, A.R. Baldwin, J.N. Kundson, J.D. Carlson, J. Rapaport, Nuclear Instruments and Methods in Physics Research Section A 151 (1978) 445.
[45] W. Tornow, W. Arnodl, J. Herdtweck, G. Mertens, Nuclear Instruments and Methods in Physics Research Section A 244 (1986) 477.
[46] R.A. Cecil, B.D. Anderson, R. Madey, Nuclear Instruments and Methods in Physics Research Section A 161 (1979) 439.
[47] W. Hansen, D. Richter, Nuclear Instruments and Methods in Physics Research Section A 476 (2002) 195.
[48] R.E. Pywell, B.D. Sawatzky, J. Ives, N.R. Kolb, R. Igarashi, W.A. Wurtz, Nuclear Instruments and Methods in Physics Research Section A 565 (2006) 725.
[49] C. Matei, F.-J. Hambsch, Nuclear Instruments and Methods in Physics Research Section A 676 (2012) 135.
[50] H. Schölermann, H. Klein, Nuclear Instruments and Methods in Physics Research Section A 169 (1980) 25.
[51] P. Sparrman, I. Lindskog, A. Marelius, Nuclear Instruments and Methods in Physics Research Section A 41 (1966) 299.
[52] E. Padovani, S.A. Pozzi, S.D. Clarke, E.C. Miller, MCNPX-PoliMi Users Manual, Technical Report, Radiation Safety Information Computational Center, Oak Ridge National Laboratory, 2012.
[53] A. Tomanin, Development of a Liquid Scintillator-Based Neutron Coincidence Counter for Safeguards Applications (Ph.D. thesis), University of Ghent, Forthcoming.
[54] H.J. Brede, M. Cosack, G. Dietze, H. Gumpert, S. Guldbakke, R. Jahr, M. Kutscha, D. Schlegel-Bickmann, H. Schölermann, Nuclear Instruments and Method in Physics Research Section A 169 (1980) 349.
[55] Laboratoire National Henri Becquerel, Recommended Data. URL ⟨http://www.nucleide.org/DDEP_WG/DDEPdata.htm⟩.
[56] S. Croft, Nuclear Instruments and Methods in Physics Research Section A 281 (1989) 103.
[57] J.P. Mason, Nuclear Instruments and Methods in Physics Research Section A 241 (1985) 207.
[58] R. Böttger, S. Guldbakke, H. Klein, H. Schölermann, H. Schuhmacher, H. Strzelczyk, Nuclear Instruments and Methods in Physics Research Section A 282 (1989) 358.
[59] G. Lövestam, EnergySet — A Programme to Calculate Accelerator Settings and Neutron Yield Data for the IRMM VdG Laboratory, Technical Report, JRC-IRMM Internal Report GER/NP/2/2002/06/20, unpublished, Geel, Belgium, 2002.
[60] E. Birgersson, G. Lövestam, NeuSDesc – Neutron Source Description Software Manual, EUR Report 23794, Technical Report, Office for Official Publications of the European Communities, Luxemburg, European Communities, 2008.
[61] H.H. Andersen, J.F. Ziegler, Hydrogen Stopping Powers and Ranges in All Elements, The stopping and ranges of ions in matter, vol. 3, Pergamon Press, New York, 1977.
[62] J.F. Ziegler, Helium Stopping Powers and Ranges in All Elements, The stopping and ranges of ions in matter, vol. 4, Pergamon Press, New York, 1977.
[63] H. Liskien, A. Paulsen, Atomic Data and Nuclear Data Tables 11 (1973) 569.
[64] H. Liskien, A. Paulsen, Atomic Data and Nuclear Data Tables 15 (1975) 57.
[65] J. Ziegler, J. Biersack, SRIM-2008. URL ⟨/http://www.srim.orgS⟩.
[66] G. Dietze, H. Klein, NRESP4 and NEFF4 Monte Carlo Codes for the Calculation of Neutron Response Functions and Detection Efficiencies for NE-213 Scintillation Detectors, Technical Report, Physikalisch-Technische Bundesanstalt (PTB), 1982.
[67] Reference Neutron Radiations Part 1: Characteristics and Methods of Production, Technical Report, International Standard ISO/DIS 8529-1, 2000.